38th Fluid Dynamics Conference and Exhibit
23 - 26 June 2008, Seattle, Washington

AIAA 2008-3748

Large Eddy Simulation of Circular Cylinder Flow by Using High Order WENO Scheme

Yiqing Shen[*], Gecheng Zha[†], Baoyuan Wang[‡]
Dept. of Mechanical and Aerospace Engineering
Miami Wind ^{TM}
University of Miami
Coral Gables, Florida 33124
E-mail: yqshen@miami.edu, gzha@miami.edu

Abstract

This paper investigates the feasibility of a high order finite difference weighted essentially nonoscillatory(WENO) scheme for large eddy simulations(LES) with implicit subgrid scale model. In this paper, the 5th-order WENO scheme with a conservative 4th-order central differencing for viscous terms are used to simulate the flow past a circular cylinder at $Re_D = 3900$. The turbulent effects near wake with different spanwise length ($1D$ and πD) are studied. The comparison of the simulations with implicit subgrid scale model and with Smagorisky SGS model is also presented.

1 Introduction

Large eddy simulation (LES) has been regarded as a viable engineering tool with rapidly enhanced computer architecture and mathematical modeling[1]. The presence of various regimes in the flow over a cylinder makes the computation of this flow an interesting and challenging task[2]. During the past decade, many large eddy simulations (LES) have been performed for subcritical Reynolds numbers, especially at $Re_D = 3900$, mainly due to the availability of the experimental results of Lourenco and Shih[3] and Ong and Wallace[4]. This flow has also been used as a benchmark case to examine theoretical issues pertaining to the application of LES in general curvilinear coordinate systems[5]. There is a general consensus that low-order upwind schemes are not able to predict correctly the base suction pressure coefficient, separation angles, and the size and structure of the recirculation zone behind the cylinder.

The two dominant subgrid-scale models for LES are Smagorisky and dynamic subgrid-scale stress models. Boris et al.[6] was the first research group to take the numerical dissipation as the SGS model. Garnier et al.[7] gave the numerical simulations of freely decaying isotropic fluid turbulence using shock-capturing schemes. The ENO, WENO, MENO, and MUSCL4 schemes let some energy reach the cut-off wavenumber and preserve the flow from energy accumulation at small scales. In this sense, they behave like a (very dissipative) SGS model. They found that the addition of a SGS model to the shock-capturing schemes tested is unnecessary and inconvenient.

---

[*] Research Scientist, AIAA Member
[†] Associate Professor, AIAA Senior Member
[‡] Ph.D. Candidate

For the flow over a circular cylinder, the large-eddy simulations with no subgrid scale model, or say, with implicit subgrid scale model, are also studied by Rizzetta et al.[8], Breuer[9], Kasliwal et al.[10]. A variety of discretization methods have been used, including spectral element method[11], B-spline method [2], sixth-order compact scheme [8], seventh-order upwind difference scheme [12], FE/spectral algorithm[13], hybrid scheme of the upwind difference scheme and the second-order central difference scheme, QUICK, and fourth-order central difference scheme[9].

Kravchenko and Moin[2] compared the results of two spanwise lengths ($\pi D/2$ and πD) with and without a subgrid scale model. They found the simulation on coarse spanwise grids appear to be in better agreement with the experiment than those from the refined calculations. There is insignificant differences between the mean velocity profiles from the simulations with and without a SGS model. The difference appears in the rms fluctuations. It was found that such a limited domain does not alter significantly the statistics in the very near wake ($x/D < 2$). The spanwise sizes effect ($\pi D/2$ and πD) are also studied by Rizzetta et al [14]. They found that the actual extent of the domain in the z direction is not critical since periodic conditions are enforced in the spanwise direction, and the solutions are spanwise averaged. The criterion is that the span must be sufficiently long such that large-scale structures are not artificially forced to become two-dimensional. It has been established by Kravchenko and Moin[2] that a spanwise extent of $\pi/2$ satisfies this constraint. The study of Rizzetta et al [14, 8] found that the distribution of the surface pressure and the mean wake centerline streamwise velocity deviate greatly from the experiment when the span is increased. Breuer[9] compared the spanwise size of $L_z = 2\pi D$ and πD, and found it did not improve the results significantly. In the study of Alkishriwi et al [15], the length in spanwise direction is taken as$1D$, the results agree very well with the experiment.

In this paper, we study the feasibility of high order weighted essentially nonoscillatory(WENO) schemes [16, 17] for LES over a circular cylinder with no explicit subgrid scale models. The turbulent effects of spanwise size ($1D$ and πD) are studied. Comparison of the simulations with implicit subgrid scale model and with Smagorisky SGS model is also presented.

2 The Numerical Method

2.1 Governing Equations

The governing equations are the spatially filtered compressible Navier-Stokes equations. The spatial filtering removes the small scale high frequency components of the fluid motion, while keeping the unsteadiness associated with the large scale turbulent motion.

For an arbitrary function $u(x_i, t)$, the filtered variable $\bar{u}(x_i, t)$ is defined as:

$$\bar{u}(x_i, t) = \int_D G(x_i - \xi_i, \Delta) u(\xi_i, t) d\xi_i \tag{1}$$

where G is the filter function and Δ is the filter width and is associated with the mesh size.

Similar to the case of RANS, for compressible flows, it is convenient to introduce the Farve-filtered variable $\tilde{u}(x_i, t)$ as:

$$\tilde{u}(x_i, t) = \frac{\overline{\rho u}}{\bar{\rho}} \tag{2}$$

A variable can be thus decomposed into its Favre-filtered component and fluctuating component as:

$$u(x_i, t) = \tilde{u}(x_i, t) + u''(x_i, t) \tag{3}$$

Applying these definitions and following the derivation of Knight et al.[18], the filtered compressible Navier-Stokes equations in Cartesian coordinates and relative frame can be expressed as:

$$\frac{\partial \mathbf{Q}}{\partial t} + \frac{\partial \mathbf{F}}{\partial x} + \frac{\partial \mathbf{G}}{\partial y} + \frac{\partial \mathbf{H}}{\partial z} = \frac{1}{Re}(\frac{\partial \mathbf{F_v}}{\partial x} + \frac{\partial \mathbf{G_v}}{\partial y} + \frac{\partial \mathbf{H_v}}{\partial z}) \tag{4}$$

where

$$\mathbf{Q} = \begin{pmatrix} \bar{\rho} \\ \bar{\rho}\tilde{u} \\ \bar{\rho}\tilde{v} \\ \bar{\rho}\tilde{w} \\ \bar{\rho}\tilde{e} \end{pmatrix}, \mathbf{F} = \begin{pmatrix} \bar{\rho}\tilde{u} \\ \bar{\rho}\tilde{u}^2 + \bar{p} \\ \bar{\rho}\tilde{u}\tilde{v} \\ \bar{\rho}\tilde{u}\tilde{w} \\ (\bar{\rho}\tilde{e} + \bar{p})\tilde{u} \end{pmatrix}, \mathbf{G} = \begin{pmatrix} \bar{\rho}\tilde{v} \\ \bar{\rho}\tilde{v}\tilde{u} \\ \bar{\rho}\tilde{v}^2 + \bar{p} \\ \bar{\rho}\tilde{v}\tilde{w} \\ (\bar{\rho}\tilde{e} + \bar{p})\tilde{v} \end{pmatrix}, \mathbf{H} = \begin{pmatrix} \bar{\rho}\tilde{w} \\ \bar{\rho}\tilde{w}\tilde{u} \\ \bar{\rho}\tilde{w}\tilde{v} \\ \bar{\rho}\tilde{w}^2 + \bar{p} \\ (\bar{\rho}\tilde{e} + \bar{p})\tilde{w} \end{pmatrix}$$

$$\mathbf{F_v} = \begin{pmatrix} 0 \\ \bar{\tau}_{xx} + \sigma_{xx} \\ \bar{\tau}_{xy} + \sigma_{xy} \\ \bar{\tau}_{xz} + \sigma_{xz} \\ Q_x \end{pmatrix}, \mathbf{G_v} = \begin{pmatrix} 0 \\ \bar{\tau}_{yx} + \sigma_{yx} \\ \bar{\tau}_{yy} + \sigma_{yy} \\ \bar{\tau}_{yz} + \sigma_{yz} \\ Q_y \end{pmatrix}, \mathbf{H_v} = \begin{pmatrix} 0 \\ \bar{\tau}_{zx} + \sigma_{zx} \\ \bar{\tau}_{zy} + \sigma_{zy} \\ \bar{\tau}_{zz} + \sigma_{zz} \\ Q_z \end{pmatrix},$$

In above equations, ρ is the density, u, v, w are the Cartesian velocity components in x, y, z directions, p is the static pressure, and e is the total energy per unit mass.The overbar denotes a regular filtered variable as given in Eq. (1), and the tilde is used to denote the Favre filtered variable defined in eq.(2).

The $\bar{\tau}$ is the molecular viscous stress tensor and is estimated as:

$$\bar{\tau}_{ij} = \frac{2}{3}\tilde{\mu}\frac{\partial \tilde{u}_k}{\partial x}_k \delta_{ij} + \mu(\frac{\partial \tilde{u}_i}{\partial x_j} + \frac{\partial \tilde{u}_j}{\partial x_i}), \qquad i, j = 1, 2, 3 \tag{5}$$

The above equation is in the tensor form, where the subscript 1, 2, 3 represent the coordinates, x, y, z and the Einstein summation convention is used.

The molecular viscosity $\tilde{\mu} = \tilde{\mu}(\tilde{T})$ is determined by Sutherland law.

The σ is the subgrid scale stress tensor due to the filtering process and is expressed as:

$$\sigma_{ij} = -\bar{\rho}(\widetilde{u_i u_j} - \tilde{u}_i\tilde{u}_j) \tag{6}$$

The energy flux Q is expressed as:

$$Q_i = \tilde{u}_j(\bar{\tau}_{ij} + \sigma_{ij}) - \bar{q}_i + \Phi_i \tag{7}$$

where Φ is the subscale heat flux:

$$\Phi_i = -C_p\bar{\rho}(\widetilde{u_i T} - \tilde{u}_i\tilde{T}) \tag{8}$$

The $\bar{q}_i$ is the molecular heat flux:

$$\bar{q}_i = -\frac{\tilde{\mu}}{(\gamma - 1)Pr}\frac{\partial a^2}{\partial x_i}$$

where $a = \sqrt{\gamma R\tilde{T}}$ is the speed of sound .

$$\bar{\rho}\tilde{e} = \frac{\bar{p}}{(\gamma - 1)} + \frac{1}{2}\bar{\rho}(\tilde{u}^2 + \tilde{v}^2 + \tilde{w}^2) + \rho k \tag{9}$$

where γ is the ratio of specific heats, ρk is the subscale kinetic energy per unit volume.

$$\rho k = \frac{1}{2}\bar{\rho}(\widetilde{u_i u_i} - \tilde{u}_i\tilde{u}_i) = -\frac{1}{2}\sigma_{ii} \tag{10}$$

In this paper, two ways are used to close of equation (4) for the subgrid scale stress σ_{ij} and heat flux Φ_{ij}. The one is to follow Boris et al[6], Rizzetta et al.[8], Breuer[9], Kasliwal et al.[10], no subgrid scale model, or say, an implicit subgrid scale model is used. Another way is to use the compressible extension of the Smagorinsky subgrid-scale stress model used in [19][20][18] [21]. The model is

$$\sigma_{ij} = 2C_R\bar{\rho}\Delta^2\sqrt{\tilde{S}_{kl}\tilde{S}_{kl}}(\tilde{S}_{ij} - \frac{1}{3}\tilde{S}_{kk}\delta_{ij}) \tag{11}$$

The rate of strain tensor is defined as

$$\tilde{S}_{ij} = \frac{1}{2}(\frac{\partial \tilde{u}_i}{\partial x_j} + \frac{\partial \tilde{u}_j}{\partial x_i}) \tag{12}$$

The eddy viscosity model for subgrid-scale heat flux

$$\Phi_i = \bar{\rho}C_p\frac{C_R}{Pr_t}\Delta^2\sqrt{\tilde{S}_{kl}\tilde{S}_{kl}}\frac{\partial \tilde{T}}{\partial x_j} \tag{13}$$

Where $C_R = 0.00423$ and $Pr_t = 0.4$ will be used [18] [21].

The filter width can be estimated as

$$\Delta = (\overline{V})^{\frac{1}{3}} \tag{14}$$

where $\overline{V}$ is the average volume of all cells which share the node. For boundary layer flows, Δ is modified by the Van Driest damping factor

$$D = 1 - e^{-y^+/A} \tag{15}$$

where A=26, $y^+ = yu_\tau/\nu_w$ is the normal distance to the wall normalized by the viscous length scale ν_w/u_τ, where ν_w is the kinematic viscosity evaluated at the wall and u_τ is the local friction velocity.

2.2 The 5th-Order WENO Scheme[16]

The finite difference 5th-order accuracy WENO scheme suggested by Jiang and Shu [16] is used. In multidimensional calculation, the finite difference WENO scheme is more efficient than the finite volumes scheme[22].

The fifth-order accurate WENO ($r = 3$) reconstruction of u^L and u^R can be written as

$$u^L_{i+1/2} = \omega_0 q_0 + \omega_1 q_1 + \omega_2 q_2$$

where

$$q_0 = \frac{1}{3}u_{i-2} - \frac{7}{6}u_{i-1} + \frac{11}{6}u_i$$

$$q_1 = -\frac{1}{6}u_{i-1} + \frac{5}{6}u_i + \frac{1}{3}u_{i+1}$$

$$q_2 = \frac{1}{3}u_i + \frac{5}{6}u_{i+1} - \frac{1}{6}u_{i+2}$$

and

$$\omega_k = \frac{\alpha_k}{\alpha_0 + \cdots + \alpha_{r-1}},$$

$$\alpha_k = \frac{C_k}{\varepsilon + IS_k}, \quad k = 0, \cdots, r-1$$

$$C_0 = 0.1, \quad C_1 = 0.6, \quad C_2 = 0.3$$

$$IS_0 = \frac{13}{12}(u_{i-2} - 2u_{i-1} + u_i)^2 + \frac{1}{4}(u_{i-2} - 4u_{i-1} + 3u_i)^2$$

$$IS_1 = \frac{13}{12}(u_{i-1} - 2u_i + u_{i+1})^2 + \frac{1}{4}(u_{i-1} - 4u_i + 3u_{i+1})^2$$

$$IS_2 = \frac{13}{12}(u_i - 2u_{i+1} + u_{i+2})^2 + \frac{1}{4}(u_i - 4u_{i+1} + 3u_{i+2})^2$$

where, ε is introduced to avoid the denominator becoming zero. In the practical applications, ε plays an important role on the convergence, stability and accuracy of WENO scheme [23, 24]. The higher the ε value, the closer for the weights to the optimum value C_k, and hence the lower the numerical dissipation. However, when there is shock in the flow, the *varepsilon* value can not be too large to maintain the sensitively to shosks. In [23, 24],$\varepsilon = 10^{-2}$ is recommended for the transonic flows with shock waves. In this paper, since there is no shock wave in the flow, we use the fixed weights $\omega_k = C_k$ to have minimum numerical dissipation. Testing with variable weights is also in progress.

The u^R will be constructed symmetrically as u^L about $i + 1/2$.

2.3 The Discretization of Viscous Terms[23, 25]

A fully conservative fourth-order accurate finite central differencing scheme developed in [23, 25] is employed for the viscous terms.

For examples,

$$\frac{\partial R}{\partial \xi}|_i = \tilde{R}_{i+1/2} - \tilde{R}_{i-1/2} \tag{16}$$

where

$$\tilde{R}_{i-1/2} = \frac{1}{24\Delta\xi}(-R_{i+1/2} + 26R_{i-1/2} - R_{i-3/2}) \tag{17}$$

$$R_{i-1/2} = [(\xi_x \tau_{xx}) + (\eta_y \tau_{xy}) + (\zeta_z \tau_{xz})]_{i-1/2}$$

$$\begin{aligned} (\tau_{xx})_{i-1/2} = \quad & \mu|_{i-1/2}\{\tfrac{4}{3}\left[(\xi_x \tfrac{\partial u}{\partial \xi})|_{i-1/2} + (\eta_x \tfrac{\partial u}{\partial \eta})|_{i-1/2} + (\zeta_x \tfrac{\partial u}{\partial \zeta})|_{i-1/2}\right] \\ & -\tfrac{2}{3}[(\xi_y \tfrac{\partial v}{\partial \xi})|_{i-1/2} + (\eta_y \tfrac{\partial v}{\partial \eta})|_{i-1/2} + (\zeta_y \tfrac{\partial v}{\partial \zeta})|_{i-1/2} \\ & (\xi_z \tfrac{\partial w}{\partial \xi})|_{i-1/2} + (\eta_z \tfrac{\partial w}{\partial \eta})|_{i-1/2} + (\zeta_z \tfrac{\partial w}{\partial \zeta})|_{i-1/2}]\} \end{aligned} \tag{18}$$

To achieve strict 4th-order accuracy, Eqs.(17)-(18) must be used. For interface $I = i-3/2, i-1/2, i+1/2$, the following formulas must be adopted.

$$\mu_I = \sum_{l=m}^{n} C_l^I \mu_{i+l}, \ m = -2, n = 1, \tag{19}$$

$$\frac{\partial u}{\partial \xi}|_I = \frac{1}{\Delta \xi}\sum_{l=r}^{s} D_l^I u_{i+l},\ r=-3, n=2, \tag{20}$$

$$\frac{\partial u}{\partial \eta}|_I = \sum_{l=m}^{n} C_l^I \frac{\partial u}{\partial \eta}|_{i+l,j},\ m=-2, n=1, \tag{21}$$

where

$$\frac{\partial u}{\partial \eta}|_{i,j} = \frac{1}{\Delta \eta}\sum_{l=p}^{q} C_l^c u_{i,j+l},\ p=-2, q=2, \tag{22}$$

The other terms are determined similarly. By choosing different ranges for $(m,n),(r,s),(p,q)$ and different coefficients C_l^I, D_l^I, C_l^c, one can obtain the different order accuracy of the viscous terms. In this paper, we take $(m,n)=(-2,1),(r,s)=(-3,2), and\ (p,q)=(-2,2)$, then $\mu_I, \frac{\partial u}{\partial \eta}|_I, \frac{\partial u}{\partial \eta}|_{i,j}$ achieve fourth-order accuracy, and $\frac{\partial u}{\partial \xi}|_I$ achieve fifth-order accuracy[23]. The coefficients C_l^I, D_l^I, C_l^c are given in Tables 1-3.

Table 1: The coefficients of C_l^I

I	C_{-2}^I	C_{-1}^I	C_0^I	C_1^I
$i-3/2$	5/16	15/16	-5/16	1/16
$i-1/2$	-1/16	9/16	9/16	-1/16
$i+1/2$	1/16	-5/16	15/16	5/16

Table 2: The coefficients of D_l^I

I	D_{-3}^I	D_{-2}^I	D_{-1}^I	D_0^I	D_1^I	D_2^I
$i-3/2$	71/1920	-141/128	69/64	1/192	-3/128	3/640
$i-1/2$	-3/640	25/384	-75/64	75/64	-25/384	3/640
$i+1/2$	-3/640	3/128	-1/192	-69/64	141/128	-71/1920

Table 3: The coefficients of C_l^c

C_{-2}^c	C_{-1}^c	C_0^c	C_1^c	C_2^c
1/12	-8/12	0	8/12	-1/12

2.4 The Time Discretization[26]

A pseudo temporal term $\frac{\partial Q}{\partial \tau}$ is added to the governing equation (4) for unsteady computations. The temporal term $\frac{\partial Q}{\partial t}$ is discretized implicitly using a 2nd-order three point, backward differencing as the following

$$\frac{\partial Q}{\partial t} = \frac{3Q^{n+1} - 4Q^n + Q^{n-1}}{2\Delta t},$$

and the pseudo temporal term is discretized with first-order Euler scheme to enhance diagonal dominance. The semi-discretized governing equation can then be expressed as

$$[(\frac{1}{\Delta \tau} + \frac{1.5}{\Delta t})I - (\frac{\partial \tilde{F}}{\partial Q})^{n+1,m}]\delta Q^{n+1,m+1} = R^{n+1,m} - \frac{3Q^{n+1,m} - 4Q^n + Q^{n-1}}{2\Delta t}, \tag{23}$$

where n is the physical time level index, m is the iteration index within a physical time step, Δt and $\Delta\tau$ are the physical and pseudo time step, $\tilde{F}$ is the net flux at the interface between 2 mesh points, respectively. Eq. (23) is solved using the unfactored Gauss-Seidel line iteration[27].

2.5 The Boundary Conditions

Steady state freestream conditions are used for the upstream portion of the outer boundary. For downstream boundary, the static pressure was specified as freestream value, and the streamwise gradients of other variables were forced to vanish. The periodic boundary condition is enforced in spanwise direction. The wall BC suggested in [23] to achieve the conservation by shifting half interval of the mesh on the wall is employed. The no slip condition is employed on the cylinder surface, for computing the flux $F_{1/2}$ on the wall, there is

$$F_{\frac{1}{2}} = \begin{bmatrix} \rho v|_w \\ \rho uv|_w \\ \rho v^2 + p|_w \\ \rho vw|_w \\ (\rho e + p)v|_w \end{bmatrix} = \begin{bmatrix} 0 \\ 0 \\ p|_w \\ 0 \\ 0 \end{bmatrix}$$

and then the third-order accuracy wall boundary formula is used for $p|_w$,

$$p_w = \frac{1}{6}(11p_1 - 7p_2 + 2p_3)$$

3 Results and Discussion

In this paper, the baseline computational domain in the azimuthal and radial directions is set as $\pi D \times 75D$, and the following cases are calculated.

Table 4: More cases in progress

Case	Mesh	Spanwise Length	SGS Model
1	$120 \times 80 \times 30$	$1D$	implicit
2	$120 \times 80 \times 90$	πD	implicit
3	$120 \times 80 \times 90$	πD	Smagorinsky
4	$240 \times 160 \times 90$	πD	implicit

The grid points are clustered near the cylinder surface in the radial direction. Same as in the Ref.[10], the first grid-point non-dimensional spacing equal to 7.7×10^{-5} is used. Fig.1 gives the grid sketch of $x - y$ plane close to the cylinder surface.

The initial flowfield is obtained by using steady computation. Then the flowfiled is simulated by using unsteady method to dimensionless time $t = 100$. The statistical results are obtained from $t = 100$ to $t = 250$. Within each physical time step, 60 pseudo time steps are used with the L_2 Norm residual reduced by 6 order of magnitude.

The mean pressure coefficient compared with the experiment along the surface of the cylinder is given in Fig. 2. For $Re = 3900$, only the measured coefficient of back pressure (at $\theta = 180^o$) is available for comparison. In the region of $\theta \subset (0, 60^o)$, the mean pressure coefficient computed in this paper is closer to the experimental data than the results computed by Kasliwal et al.[10], which uses finer mesh size of $100\times100\times30$ and a fourth-order compact difference scheme. The results of case 2 and case 3 ($L_z = \pi D$, with implicit and explicit SGS model) agree very well with the experiments in the whole domain $\theta \subset (0, 180^o)$, both results are basically identical. The case 4 with the finer grid in the azimuthal and radial directions overpredicts the pressure coefficient, similar to the result of DNS and LES obtained by Rizzetta et al [14], in which a 6th order compact scheme and the mesh size of $199 \times 197 \times 53$ are used. The difference between case 2 and case 4 shows that the LES with implicit SGS model is sensitive to mesh size.

Fig. 3 shows the mean streamwise velocity on the centerline in the wake of the cylinder, which demonstrates that, when $x/D < 2$, case 1 agrees best with the experiment of Krothapalli[28], the computed velocity by the other two groups[2, 10] is significantly under predicted. At $x/D > 3$, case 1 agrees very well with the experiment of Ong and wallace[4]. With $L_z = \pi D$, case 2 and case 3 agree better with experiment than others in the region of $2.5 < x/D < 4.5$, and the velocity is overpredicted when $x/D > 4.5$. Execpt the slight difference near $x/D = 4$, case 2 and case 3 are basically identical. With the refined grid, case 4 obtains the similar results to the DNS of case A ($L_z = \pi D$) of Rizzetta et al [14], which is deviated from the experiment quite significantly.

Figs. 4 and 5 give the distributions of the mean streamwise velocity and the mean crossflow velocity for three streamwise locations, $x/D = 1.06, x/D = 1.54$ and $x/D = 2.02$. Case 1 agrees very well with the computed results of Krachenko and Moin[2] and Kasliwal et al[10]. At $x/D = 2.02$, case 4 predicts the lowest mean streamwise velocity. In the middle of $x/D = 1.54$, similar to $x/D = 1.06$, the distribution of mean cross velocity with $L_z = \pi D$ (case 2, 3, and 4) has a wavy shape. But the results with $L_z = 1D$ (case 1) at $x/D = 1.54$ and $x/D = 2.02$ vary smoothly. That is to say, with different spanwise length, the variation region of mean cross velocity is different. In the region from $x/D = 1.06$ to $x/D = 1.54$, the mean cross velocity with $L_z = \pi D$ hold its wavy shape; but the result with $L_z = 1D$ changes from a wavy shape to a smooth line. The inversed phenomena takes place in the region from $x/D = 1.54$ to $x/D = 2.02$. Comparing the mean cross velocity with the simulations of Kravchenko and Moin[2] and Rizzetta et al [14], we can find that our simulation with $L_z = 1D$ is similar to that of Kravchenko and Moin, and the simulation with $L_z = \pi D$ is similar to that of Rizzetta et al. In the two figures, case 2 and case 3 are essentially identical, this shows that the SGS model has little effect on the averaged velocity.

Figs. 6-8 compare Reynolds stresses. For these Reynolds stress, case 1 with $L_z = 1D$ agree much better with experiment than the other cases with $L_z = \pi D$. Case 2 (with implicit SGS model) and case 3 (with SGS model) has little difference. For the refined mesh, the simulated Reynolds stresses (with implicit SGS model) is decreased. From Fig.7, it can be seen that the simulated shear Reynolds stresses with $L_z = \pi D$ vary wavily.

Fig. 9 is the contours of instantaneous kinetic energy of case 1, which shows that the flow is mostly laminar from the leading edge to $\theta = 45^o$. Then the transition occur at about $\theta = 45^o$. After $\theta = 65^o$, the flow is mostly turbulent due to the vortex shedding.

The instantaneous vorticity is plotted in Fig.10, which shows that some small scale structures are captured.

Figs. 11-14 give the temporal variations of three velocity components u, v, w of case 1 at three locations indicted in Fig.11. The probes are located in $(0.2724, -0.4195, 0.5)$, $(0.5091, 0.1654, 0.5)$, and $(3..6225, -0.7700, 0.5)$, respectively.

4 Conclusion

This paper used the 5th-order WENO scheme and a conservative 4th-order central differencing scheme to conduct a large eddy simulation of the turbulent flow passing a circular cylinder. It found that the spanwise length varied from D to πD affects the flowfield structure, especially on the mean crosswise velocity, and it results in different turbulent Reynolds stress. For a large eddy simulation with implicit SGS model, the result is sensitive to mesh size. In our computation, when the mesh is refined, the Reynolds stress is decreased. The numerical results have a conclusion different from Kravchenko and Moin[2], that is, for the same mesh density, the spanwise size also affects the flow statistics in the very near wake region. The spanwise size of $1D$ yields the best agreement with the experimental data.

5 Acknowledgment

This work is supported by ARO/AFOSR Grant 50827-RT-ISP monitored by Dr Rhett Jefferies and Jenny Haire and is supported by Miami Wind ^{TM}.

References

[1] P. Moin, "Advances in large eddy simulation methodology for complex flows," *Int.J.Heat Fluid Flow*, vol. 23, p. 710, 2002.

[2] G. Kravchenko, P. Moin , " Numerical studies of flow over a circular cylinder at $Re_D = 3900$," *Phys.Fluids* , vol. 12, pp. 403–417, 2000.

[3] L.M. Lourenco, C. Shih , " Characteristics of the plane turbulent near wake of a circular cylinder, A particle image velocity study ." private communication by Beaudan and Moin (data taken from[**?**]), 1993.

[4] L. Ong, J. Wallace , " The velocity field of the turbulent very near wake of a circular cylinder ," *Exp.Fluids* , vol. 20, p. 441, 1996.

[5] Chunlei Liang, George Papadakis , " Large eddy simulation of pulsating flow over a circular cylinder at subcritical Reynolds number ," *Computer& Fluids* , vol. 36, pp. 299–312, 2007.

[6] J. Boris, F. Grinstein, E. Oran, and R. Kolbe, "New Insights into Large Eddy Simulation," *Journal of Fluid Mechanics*, vol. 41, pp. 453–480, 1970.

[7] E. Garnier, M. Mossi, P. Sagaut, P. Comte, M. Deville , " On the use of shock-capturing schemes for large-eddy simulation ," *J.Comput.Phys.* , vol. 153, pp. 273–311, 1999.

[8] D.P. Rizzetta, M.R. Visbal, G.A. Blaisdell, " A time-implicit high-order compact differencing and flitering scheme for Large-eddy simulation ," *Int.J.Numer.Meth.Fluids* , vol. 42, pp. 665–693, 2003.

[9] M. Breuer , " Numerical and modeling influences on large eddy simulations for the flow past a circular cylinder ," *Int.J.Heat Fluid Flow* , vol. 19, p. 512, 1998.

[10] A. Kasliwal, K. Ghia, U. Ghia , " Higher-order accurate solution for flow past a circular cylinder at $Re = 13,4000$." AIAA-2005-1123, 43rd AIAA Aerospace Sciences Meeting and Exhibit, Reno, Nevada,10-13 Jan., 2005.

[11] H.M. Blackburn, S. Schmidt , " Large eddy simulation of flow past a circular cylinder ." 14th Australasian Fluid Mechanics Conference, Adelaide University, Adelaide, Australia, 10-14 Dec, 2001.

[12] P. Beaudan, P. Moin , " Numerical experiments on the flow past a circular cylinder at a sub-critical Reynolds number ." Report No.TF-62, Department of Mechanical Engineering, Stanford University, 1994.

[13] D.O. Snyder, G. Degrez, " Large-eddy simulation with complex 2-D geometries using a parallel finite-enement/spetral algorithm ," *Int.J.Numer.Meth.Fluids* , vol. 41, pp. 1119–1135, 2003.

[14] G. B. D.P. Rizzetta, M.R. Visbal, "Application of a high-order compact difference scheme to large-eddy and direct numberical simulation." AIAA-99-3714, 1999.

[15] N. Alkishriwi, M. Meinke, W. Schroder, "A large-eddy simulation method for low Mach number flows using preconditioning and multigrid," *Computers & Fluids*, vol. 35, pp. 1126–1136, 2006.

[16] G.S. Jiang, and C.W. Shu, "Efficient implementation of weighted ENO schemes," *J.Comput.Phys.*, vol. 126, pp. 202–228, 1996.

[17] D.S. Balsara and C.-W. Shu, "Monotonicity Preserving weighted essentially non-oscillatory schemes with increasingly high order of accuracy," *J.Comput.Phys.*, vol. 160, pp. 405–452, 2000.

[18] D. Knight, G. Zhou, N. Okong'o, and V. Shukla, "Compressible Large Eddy Simulation Using Unstructured Grids." AIAA Paper 98-0535, 1998.

[19] G. Erlebacher, M. Hussaini, C. Speziale, and T. Zang, "Toward the Large-Eddy Simulation of Compressible Turbulent Flows," *Journal of Fluid Mechanics*, vol. 238, pp. 155–185, 1992.

[20] A. Ansari and W. Strang, "Large-Eddy Simulation of Turbulent Mixing Layers." AIAA Paper 96-0684, 1996.

[21] G. Urbin, D. Knight, and A. Zheltovodov, "Compressible Large Eddy Simulation Using Unstructured Grid: Supersonic Turbulent Boundary Layer and Compression Corner." AIAA Paper 99-0427, 1999.

[22] C.W. Shu, "Essentially non-oscillatory and weighted essentially non-oscillatory schemes for hyperbolic conservation laws." NASA/CR-97-206253, ICASE Report No.97-65, Nov. 1997.

[23] Y.Q. Shen, B.Y. Wang,and G.C. Zha, "Implicit WENO scheme and high order viscous formulas for compressible flows." AIAA-paper 2007-4431, June 2007.

[24] Y.Q. Shen, G.C. Zha, and B.Y. Wang, "Improvement of the stability and accuracy of implicit WENO scheme for transonic flows." Submitted to AIAA J., 2007.

[25] Y. Shen, G. Zha, X. Chen, " High Order Conservative Differencing for Viscous Terms and the Application to Vortex-Induced Vibration Flows." AIAA-2008-4059, 2008.

[26] X. Chen and G.-C. Zha, "Fully coupled fluid-structural interactions using an efficient high solution upwind scheme," *Journal of Fluid and Structure*, vol. 20, pp. 1105–1125, 2005.

[27] Y.Q. Shen, B.Y. Wang,and G.C. Zha, "Comparison Study of Implicit Gauss-Seidel Line Iteration Method for Transonic Flows." AIAA-paper 2007-4332, June 2007.

[28] A. Krothapalli, C. Shih, and L. Lourenco, " The near wake of a circular cylinder at $0.3 < M_\infty < 0.6$: a PIV study ." 32nd Aero Sciences Meeting and Exhibit, AIAA Paper 94-0063, 1994.

[29] C. Norberg , " Effects of Reynolds number, low-intensity free-stream turbulence on the flow around a circular cylinder ." Publ.No.87/2,Department of Applied Themoscience and Fluid Mechanics, Chalmer University of Technology, Gothenberg, Sweden, 1987.

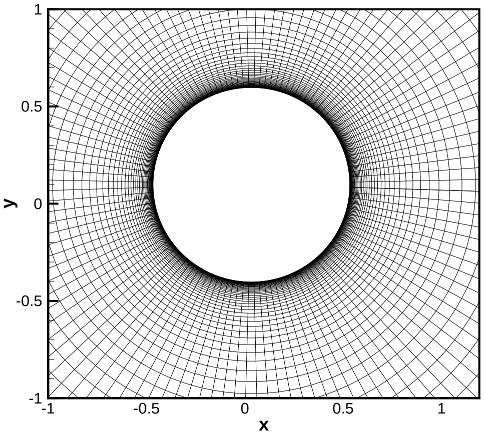

Figure 1: Sketch of mesh in $x - y$ plane

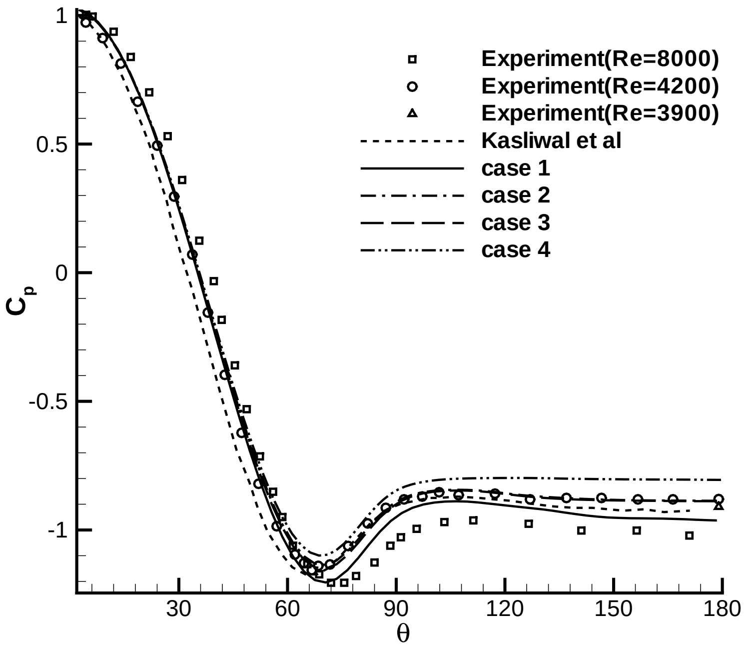

Figure 2: Mean pressure coefficient variation on the surface of the cylinder. Experiment is from Norberg[29]

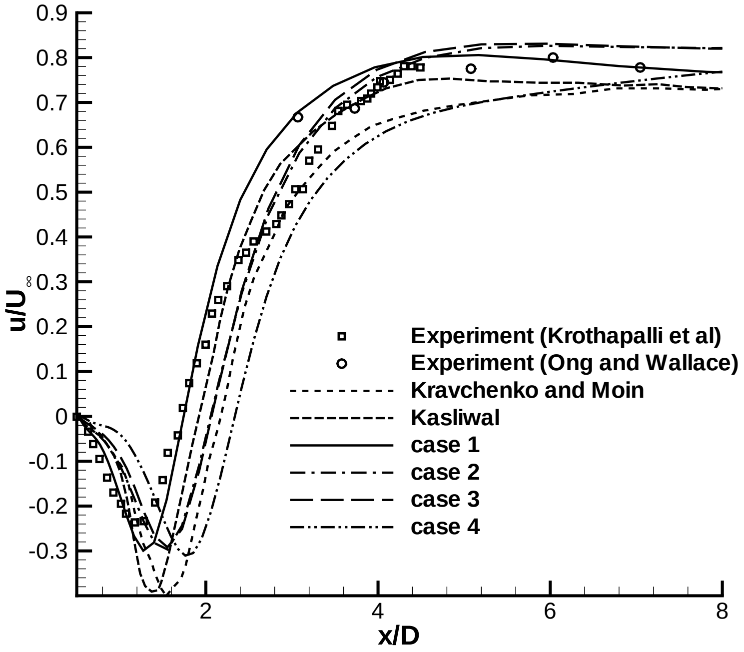

Figure 3: Mean streamwise velocity on the centerline in the wake of the cylinder

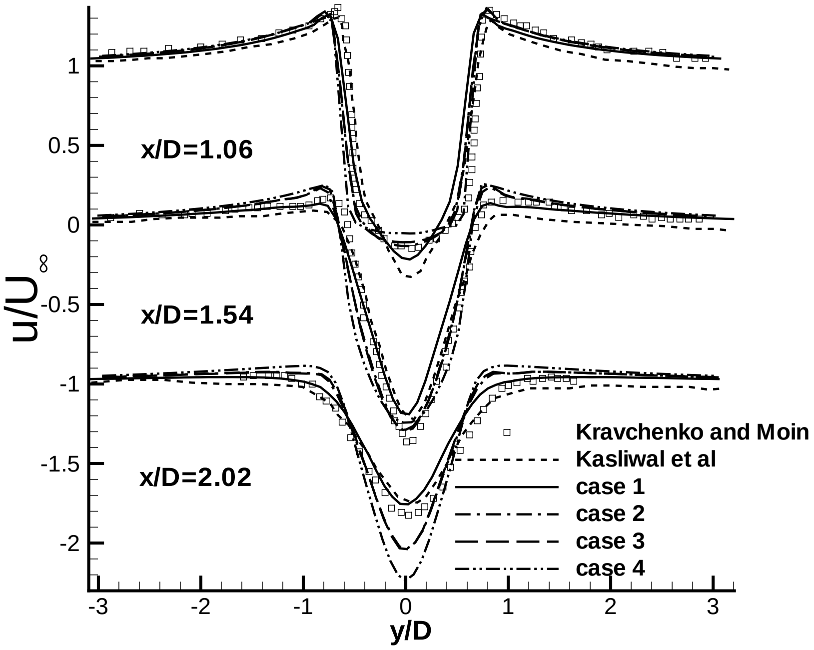

Figure 4: Mean streamwise velocity profiles at three locations in the wake of the cylinder

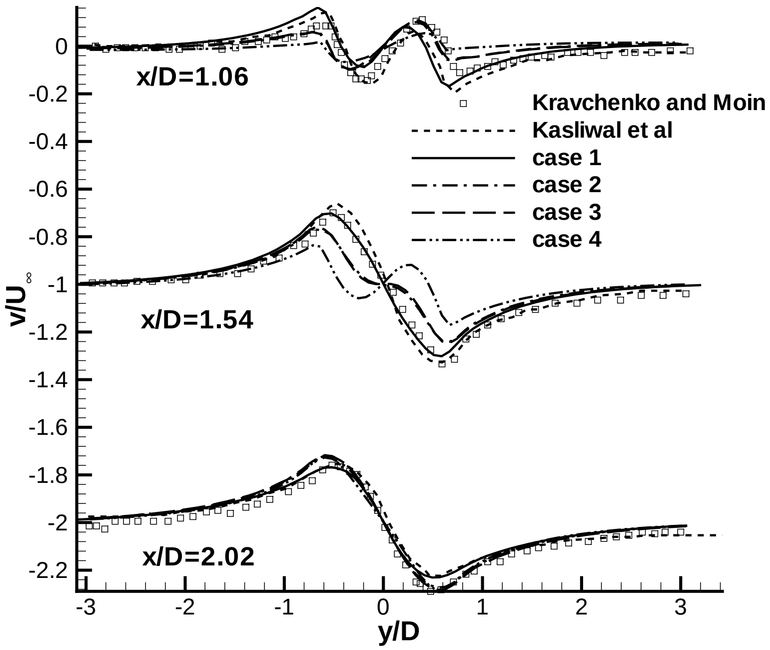

Figure 5: Mean crossflow velocity profiles at three locations in the wake of the cylinder

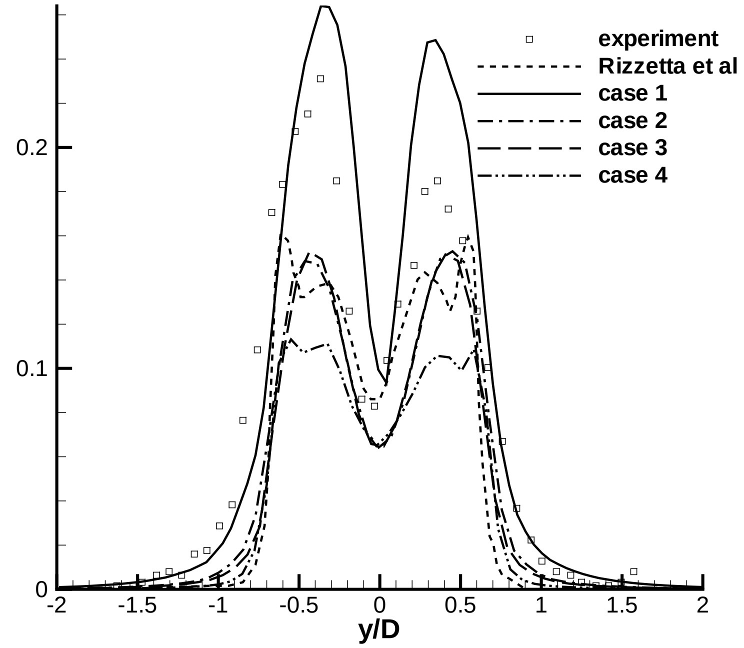

Figure 6: Streamwise Reynolds Stress in the $x/D = 1.54$ Plane

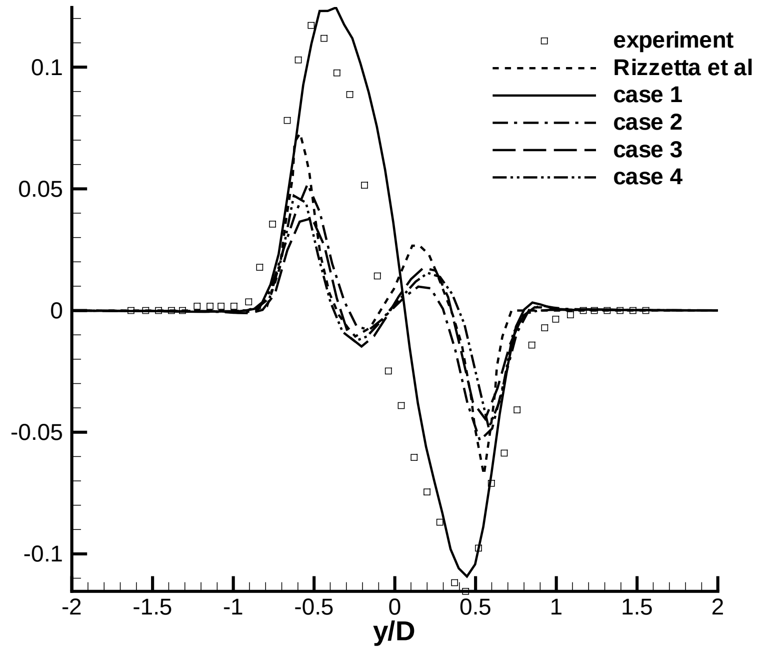

Figure 7: Shear Reynolds Stress in the $x/D = 1.54$ Plane

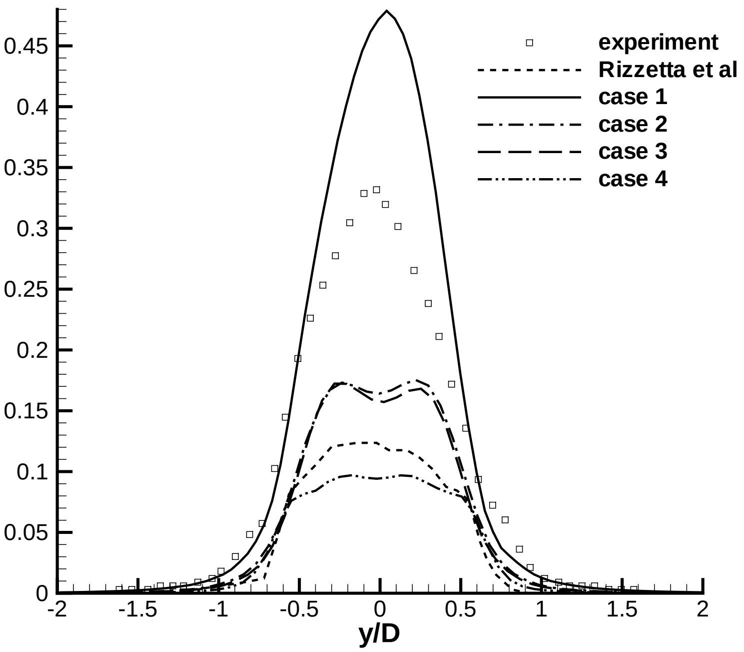

Figure 8: Lateral Reynolds Stress in the $x/D = 1.54$ Plane

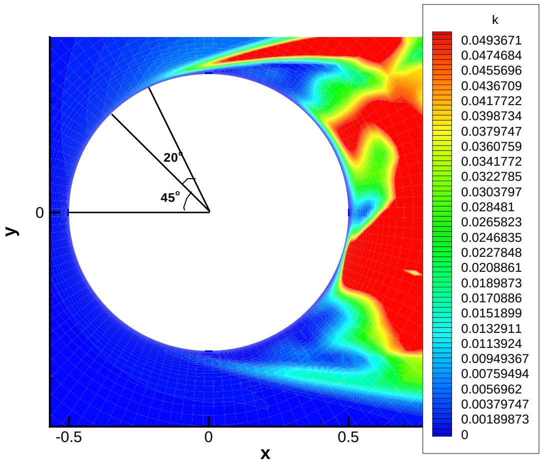

Figure 9: Contours of instantaneous kinetic energy, case 1

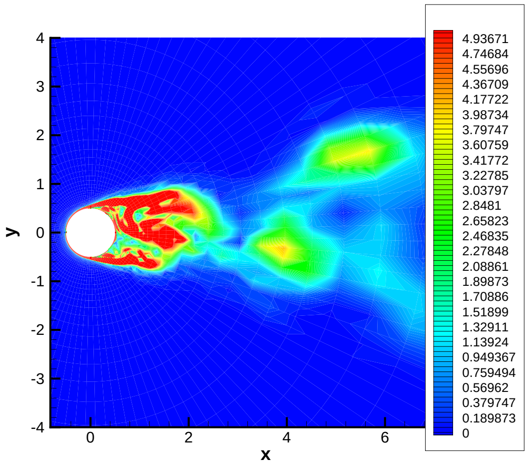

Figure 10: Contours of instantaneous vorticity, case 1

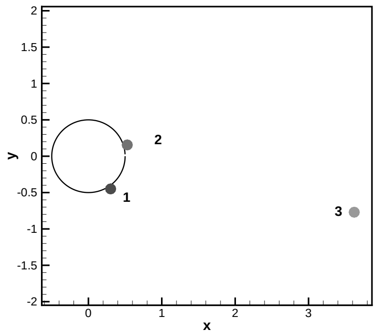

Figure 11: Probe locations where time history is tracted

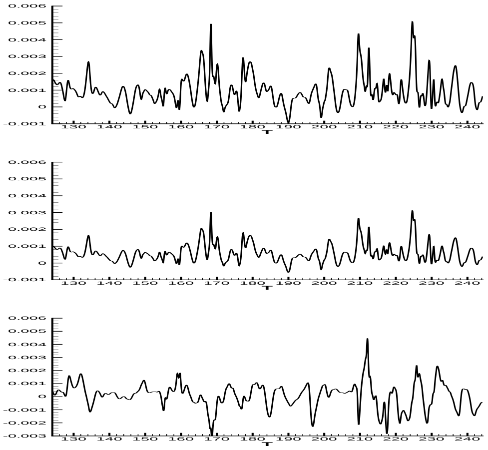

Figure 12: Velocity time history, point-1

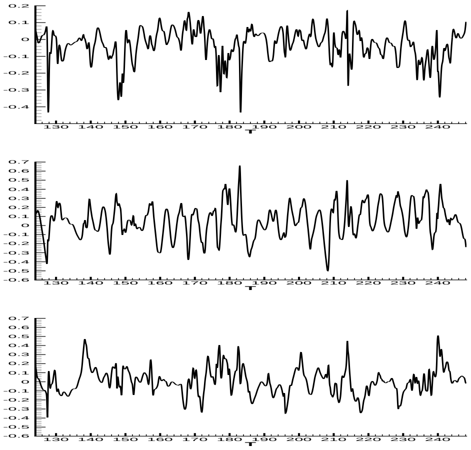

Figure 13: Velocity time history, point-2

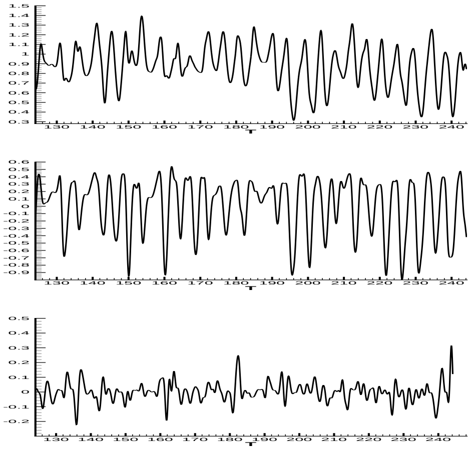

Figure 14: Velocity time history, point-3